Augmented moment method for stochastic ensembles with delayed couplings. I. Langevin model

Hideo Hasegawa*
Department of Physics, Tokyo Gakugei University, Koganei, Tokyo 184-8501, Japan
(Received 18 November 2003; revised manuscript received 2 April 2004; published 27 August 2004)

By employing a semianalytical dynamical mean-field approximation theory previously proposed by the author [H. Hasegawa, Phys. Rev. E **67**, 041903 (2003)], we have developed an augmented moment method (AMM) in order to discuss dynamics of an N-unit ensemble described by Langevin equations with delays. In an AMM, original N-dimensional *stochastic* delay differential equations (SDDEs) are transformed to infinite-dimensional *deterministic* DEs for means and correlations of local as well as global variables. Infinite-order DEs arising from the non-Markovian property of SDDE, are terminated at the finite level m in the level-m AMM (AMMm), which yields $(3+m)$-dimensional deterministic DEs. Model calculations have been made for linear and nonlinear Langevin models. The stationary solution of AMM for the linear Langevin model with $N=1$ is nicely compared to the exact result. In the nonlinear Langevin ensemble, the synchronization is shown to be enhanced near the transition point between the oscillating and nonoscillating states. Results calculated by AMM6 are in good agreement with those obtained by direct simulations.

DOI: 10.1103/PhysRevE.70.021911 PACS number(s): 87.10.+e, 84.35.+i, 05.45.−a, 07.05.Mh

I. INTRODUCTION

The time delay plays an important role in many systems such as optical devices [1] and physiological [2] and biological [3] systems. The effect of time delays has been theoretically studied by using the time-delay differential equations (DEs). Its exposed behavior includes the multistability and the bifurcation leading to chaos. It is well known that noise also plays important roles in these systems, and its effects have been thoroughly investigated with the use of stochastic DEs. One of its representative phenomena is the stochastic resonance [4], in which the signal-to-noise ratio is enhanced for subthreshold signals.

In real systems, both noises and time delays coexist, and the combined effect may be described by stochastic delay differential equation (SDDE). For instance, SDDEs are used in optics [5] and physiology [6] to model noise-driven systems exhibiting delay feedback. In recent years, there has been a growing interest in combined effects of noise and delay. The theory for SDDE remains much less studied and has been a subject of several recent papers [7–14], in which the stability condition for the equilibrium solution of linear delay Langevin equation has been studied. Its stationary solution is investigated by using the step by step method [7] and the moment method [8]. The Fokker-Planck equation (FPE) method is applied to SDDE in the limit of a small delay [9]. These studies have been confined to the stationary solution of SDDE. More interesting is, however, expected to be its dynamics in a stochastic system with a large time delay.

Real physiological and biological systems usually consist of many elements, each of which is described by SDDE. A typical example is a living brain, in which a small cluster contains thousands of similar neurons. Each neuron which is subject to various kinds of noises, receives spikes from hundreds of other neurons through dendrites with a transmission delay and generates spikes propagating along axons. Theoretical study on such coupled, stochastic systems has been made by using direct simulations (DSs) [15–17] and analytical methods like FPE [18]. Since the time to simulate such systems by conventional methods grows as N^2 with N, the size of the ensemble, it is rather difficult to simulate systems with the realistic size of $N\sim 100-1000$. Although FPE is a powerful method in dealing with the stochastic DE, a simple application of FPE to SDDE fails because of the non-Markovian property of SDDE: an evaluation of the probability density at the time t requires prior knowledge of the conditional probability density between times of t and $t-\tau$, τ being the delay time.

Quite recently the present author [19,20] proposed a dynamical mean-field approximation (DMA) as a semianalytical method dealing with large-scale ensembles subject to noises, extending the moment method [21–23]. DMA has been first applied to an N-unit ensemble described by the FitzHugh-Nagumo (FN) neuron model without time delays [24], for which original $2N$-dimensional stochastic DEs are transformed to eight-dimensional deterministic DEs for moments of local and global variables [19]. In a subsequent paper [20], DMA is applied to an N-unit general neuron ensemble, each of which is described by coupled K-dimensional DEs, transforming KN-dimensional DEs to $N_{\rm eq}$-dimensional DEs where $N_{\rm eq}=K(K+2)$. In the case of the Hodgkin-Huxley (HH) model with $K=4$ [25], we get $N_{\rm eq}=24$. The spiking-time precision and the synchronization in FN and HH neuron ensembles have been studied as functions of the noise intensity, the coupling strength and the ensemble size. The feasibility of DMA has been demonstrated in Refs. [19] and [20].

The purpose of the present paper is to apply DMA to Langevin ensembles with delays, which are expected to be good models representing not only interconnected neural net-

*Email address: hasegawa@u-gakugei.ac.jp

works but also social and technological ones. When DMA is applied to ensembles described by linear and nonlinear Langevin equations with delays, the original N-dimensional stochastic DEs are transformed to the infinite-dimensional deterministic DEs for means and correlation functions of local and global variables. Infinite-order recursive DEs arising from the non-Markovian property of SDDE, are terminated at the finite level m in our approximate method, which is hereafter referred to as the *augmented moment method* (AMM). We may study dynamics and synchronization of linear and nonlinear Langevin ensembles with delayed couplings, and examine the validity of AMM whose results are compared to results of DSs. In particular, for the linear Langevin model with $N=1$, a comparison is possible with the exact stationary solution [7].

The paper is organized as follows. In Sec. II, we describe the adopted model and method to derive the infinite-dimensional deterministic DEs from the original N-dimensional stochastic DEs. Infinite-order recursive DEs are terminated at the finite level m in the level-m AMM (AMMm). Model numerical calculations for the linear Langevin model are reported in Sec. III A, where calculated results of AMM6 for $N=1$ are nicely compared to exact solutions available for the stationary state [7]. Our AMM is compared also to the small-delay approximation (SDA) [9] which is valid for a very small delay. In Sec. III B, we present model calculations for the nonlinear Langevin model in which the stable oscillation is induced by an applied spike for an appreciable delay. The synchronization in the ensemble is investigated. It is shown that results of AMM6 are in good agreement with those of DSs. The final Sec. IV is devoted to conclusions and discussions. In a following paper [26], our AMM has been applied to ensembles described by the noisy FN neuron model with delayed couplings.

II. ENSEMBLES DESCRIBED BY THE LANGEVIN MODEL: BASIC FORMULATION

Dynamics of a Lanvegin ensemble with delayed couplings is assumed to be described by

$$\frac{dx_i(t)}{dt} = F(x_i(t)) + \frac{w}{N}\sum_j H(x_j(t-\tau)) + \xi_i(t) + I^{(e)}(t),$$

$$(i = 1 \text{ to } N) \tag{1}$$

with

$$I^{(e)}(t) = A\Theta(t - t_{\text{in}})\Theta(t_{\text{in}} + T_w - t). \tag{2}$$

Here $F(x)$ and $H(x)$ are functions of x, whose explicit forms will be shown later [Eqs. (18), (19), (29), (30), (43), and (44)]. We have assumed uniform all-to-all couplings of w and time delays of τ. The former assumption has been widely employed in many theoretical studies. The latter assumption may be justified in certain neural networks [27]. White noises of $\xi_i(t)$ are given by $\langle \xi_i(t)\rangle = 0$ and $\langle \xi_i(t)\xi_j(t')\rangle = \beta^2\delta_{ij}\delta(t-t')$ with the noise intensity of β [28]. An applied input of $I^{(e)}(t)$ given by Eq. (2) triggers oscillations in ensembles when model parameters are appropriate, as will be shown in Sec. III, $\Theta(t)$ denoting the Heaviside function, A the magnitude, t_{in} the input time, and T_w the spike width.

In DMA [19], the global variable is given by

$$X(t) = \frac{1}{N}\sum_i x_i(t), \tag{3}$$

with which we define means and correlation functions given by

$$\mu(t) = \langle X(t)\rangle, \tag{4}$$

$$\gamma(t,t') = \frac{1}{N}\sum_i \langle \delta x_i(t)\,\delta x_i(t')\rangle, \tag{5}$$

$$\rho(t,t') = \langle \delta X(t)\,\delta X(t')\rangle, \tag{6}$$

using $\delta x_i(t) = x_i(t) - \mu(t)$ and $\delta X(t) = X(t) - \mu(t)$.

In deriving equations of motion of means and variances, we have assumed that the noise intensity is weak and that the state variables obey the Gaussian distributions around their means, as in Refs. [19,20]. Numerical simulations have shown that for weak noises, the distribution of the state variable of an active rotator model nearly obeys the Gaussian distribution, although for strong noises, its distribution deviates from the Gaussian [23]. Similar behavior has been reported also in FN [22,23] and HH neuron models [29,30].

After some manipulations, we get DEs for $\mu(t)$, $\gamma(t,t)$, and $\rho(t,t')$ given by (for details see Appendix A),

$$\frac{d\mu(t)}{dt} = g_0(t) + wu_0(t-\tau) + I^{(e)}(t), \tag{7}$$

$$\frac{d\gamma(t,t)}{dt} = 2g_1(t)\gamma(t,t) + 2wu_1(t-\tau)\rho(t,t-\tau) + \beta^2, \tag{8}$$

$$\frac{d\rho(t,t)}{dt} = 2g_1(t)\rho(t,t) + 2wu_1(t-\tau)\rho(t,t-\tau) + \frac{\beta^2}{N}, \tag{9}$$

$$\begin{aligned}\frac{d\rho(t,t-m\tau)}{dt} &= [g_1(t) + g_1(t-m\tau)]\rho(t,t-m\tau) \\ &\quad + wu_1(t-(m+1)\tau)\rho(t,t-(m+1)\tau) \\ &\quad + wu_1(t-\tau)\rho(t-\tau,t-m\tau) + \frac{\beta^2}{N}\Delta(m\tau), \\ &\quad (\text{for } m \geqslant 1)\end{aligned} \tag{10}$$

with

$$g_0(t) = \sum_{n=0}^{\infty} \frac{F^{(2n)}(t)}{n!}\left(\frac{\gamma(t,t)}{2}\right)^n, \tag{11}$$

$$g_1(t) = \sum_{n=0}^{\infty} \frac{F^{(2n+1)}(t)}{n!}\left(\frac{\gamma(t,t)}{2}\right)^n, \tag{12}$$

$$u_0(t) = \sum_{n=0}^{\infty} \frac{H^{(2n)}(t)}{n!}\left(\frac{\gamma(t,t)}{2}\right)^n, \tag{13}$$

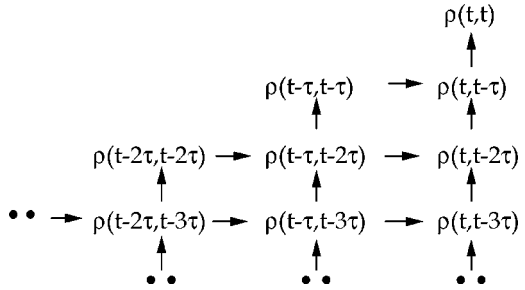

FIG. 1. The recursive structure of equations of motions $\rho(t,t)$ in AMM, arrows denoting the mutual dependence (see text).

$$u_1(t) = \sum_{n=0}^{\infty} \frac{H^{(2n+1)}(t)}{n!} \left(\frac{\gamma(t,t)}{2} \right)^n, \tag{14}$$

where $\Delta(x)=1$ for $x=0$ and 0 otherwise. Equations (7)–(10) show that an equation of motion of $\rho(t,t-\tau)$ includes new terms of $\rho(t-\tau,t-\tau)$ and $\rho(t,t-2\tau)$, which arise from the non-Markovian property of SDDE. The recursive structure of DEs for $\rho(t,t)$ is schematically expressed in Fig. 1, where arrows express the mutual dependence: $\rho(t,t)$ depends on $\rho(t,t-\tau)$, and $\rho(t,t-\tau)$ depends on $\rho(t,t-2\tau)$ and $\rho(t-\tau,t-\tau)$, and so on. Then DMA transforms the original N-dimensional SDDEs given by Eqs. (1) and (2) to the infinite-dimensional deterministic DEs given by Eqs. (7)–(10).

In actual numerical calculations, we will adopt the level-m approximation (AMMm) in which DEs are terminated at the finite level m:

$$\rho(t,t-(m+1)\tau) = \rho(t,t-m\tau). \tag{15}$$

As will be shown later in model calculations with changing m, the calculated result converges at a rather small m [Figs. 2(a) and 9(b)].

We note that the noise contribution is β^2 in Eq. (8) and it is β^2/N in Eq. (9). It is easy to get

$$\rho(t,t) = \frac{\gamma(t,t)}{N} \quad \text{for } w/\beta^2 \to 0, \tag{16}$$

$$= \gamma(t,t) \quad \text{for } \beta^2/w \to 0. \tag{17}$$

Equation (16) is consistent with the central-limit theorem. We will show later that with varying model parameters, the ratio of $\rho(t,t)/\gamma(t,t)$ is varied, which leads to a change in the synchronization of ensembles [Eq. (27)].

DSs have been performed for Eqs. (1) and (2) by using the fourth-order Runge-Kutta method with a time step of 0.01. Initial values of variables at $t \in (-\tau,0]$ are $x_i(t)=x^*$ for $i=1$ to N, where x^* is the stationary solution for $\beta=0$. The trial number of DSs to be reported in the next Sec. III is $N_r=100$ otherwise noticed. AMM calculations have been performed for Eqs. (7)–(10) with Eq. (15) by using also the fourth-order Runge-Kutta method with a time step of 0.01. Initial values are $\mu(t)=x^*$ and $\gamma(t,t)=0$ at $t \in [-\tau,0]$, and $\rho(t,t')=0$ at $t \in [-\tau,0]$ and $t' \in [-\tau,0] (t \geqslant t')$. All calculated quantities are dimensionless.

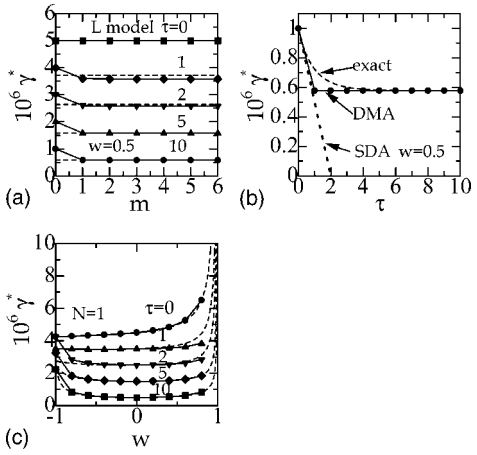

FIG. 2. (a) The stationary solution of $\gamma(t,t)$, γ^*, of the linear (L) model given by Eqs. (18) and (19) calculated in AMM m with changing the level m (solid curves) and in the exact calculation (dashed lines) for various τ with $a=1$, $w=0.5$, $\beta=0.001$, and $N=1$. (b) The τ dependence of γ^* in AMM6 (the solid curve), SDA (the dotted curve), and exact calculations (the dashed curve) for $a=1$, $w=0.5$, $\beta=0.001$, and $N=1$. (c) The w dependence of γ^* for various τ in AMM6 (solid curves) and exact calculations (dashed curves) for $\beta=0.001$ and $N=1$. Results are multiplied by a factor of 10^6, and those of $\tau=5$, 2, 1, and 0 in (a) and (c) are successively shifted upwards by 1.

III. MODEL CALCULATIONS

A. Linear model

We first consider the linear (L) model given by

$$F(x) = -ax \quad (a \geqslant 0), \tag{18}$$

$$H(x) = x. \tag{19}$$

The stability of the stationary solution of Eqs. (1), (18), and (19) with $N=1$ and $I^{(e)}(t)=0$ was discussed in Refs. [7–13], in particular, with the use of the moment method by Mackey and Nechaeva [8]. When Eqs. (18) and (19) are adopted, Eqs. (7)–(10) become

$$\frac{d\mu(t)}{dt} = -a\mu(t) + w\mu(t-\tau) + I^{(e)}(t), \tag{20}$$

$$\frac{d\gamma(t,t)}{dt} = -2a\gamma(t,t) + 2w\rho(t,t-\tau) + \beta^2, \tag{21}$$

$$\frac{d\rho(t,t)}{dt} = -2a\rho(t,t) + 2w\rho(t,t-\tau) + \frac{\beta^2}{N}, \tag{22}$$

$$\frac{d\rho(t,t-m\tau)}{dt} = -2a\rho(t,t-m\tau) + w\rho(t,t-(m+1)\tau) + w\rho(t-\tau,t-m\tau) + \left(\frac{\beta^2}{2}\right)\Delta(m\tau), \quad (\text{for } m \geqslant 1) \tag{23}$$

because $g_0(t)=-a\mu(t)$, $g_1(t)=-a$, $u_0(t)=\mu(t)$ and $u_1(t)=1$ in Eqs. (11)–(14).

For $\beta=0$ and $I^{(e)}(t)=0$, Eq. (20) has the stationary solution of $\mu^*=0$. Linearizing $\mu(t)$ around μ^*, we get the condition for the stationary solution given by

$$\tau < \tau_c = \frac{\cos^{-1}(a/w)}{\sqrt{w^2-a^2}}, \tag{24}$$

which is just the same as the $N=1$ case [8].

1. N=1 case

First we discuss model calculations for $N=1$, for which the exact solution of its stationary state is available. From Eqs. (21) and (22), we get $\rho(t,t')=\gamma(t,t')$ in the case of $N=1$. Solid curves in Fig. 2(a) express γ^*, the stationary value of $\gamma(t,t)$, when the level m in AMMm is varied for $a=1$, $w=0.5$, and $\beta=0.001$, whereas dashed curves denote the exact result given by [7]

$$\gamma^* = \left(\frac{w\sinh(\tau d)-d}{2d[w\cosh(\tau d)-a]}\right)\beta^2 \quad \text{for } |w|<a, \tag{25}$$

where $d=\sqrt{a^2-w^2}$. Equation (25) yields $10^6\gamma^*=1.0$, 0.724, 0.635, 0.581, and 0.577 for $\tau=0$, 1, 2, 5, and 10, respectively. Figure 2(a) shows that for $\tau=0$, the result of AMM agrees with the exact one for $m\geqslant 0$. In the case of $\tau=1$, the result of AMM is larger than the exact one for $m=0$, but the former is smaller than the latter for $m\geqslant 1$. This is the case also for $\tau=2$. In contrast, in cases of $\tau=5$ and 10, the results of AMM are in good agreement with the exact ones for $m\geqslant 1$. It is surprising that the results of AMM converge at a small $m(\sim 1)$.

Solid and dashed curves in Fig. 2(b) show the τ dependence of γ^* of AMM6 and the exact result, respectively (hereafter we show results in AMM6). The result of AMM is in a fairly good agreement with the exact one for $\tau>4$. It is interesting to make a comparison with results calculated by the small-delay approximation (SDA) initiated in Ref. [9], some details of SDA being given in Appendix B. The dotted curve in Fig. 2(b) expresses γ^* calculated in SDA for $w=0.5$, $\beta=0.001$, and $N=1$. Although the result of SDA agrees with the exact one at very small τ (~ 0), it shows a significant deviation from the exact one at $\tau>2$, where γ^* becomes negative violating its positive definiteness.

Solid and dashed curves in Fig. 2(c) express the w dependence of γ^* of AMM and exact ones, respectively, for various τ values with $\beta=0.001$ and $N=1$. We note that an agreement between AMM and exact results is good except for $w>0.6$ with $\tau=1-2$ and for $w<-0.8$ with $\tau=2-10$. From the results shown in Figs. 2(a)–2(c), we may say that AMM is a good approximation for a large τ $(\geqslant 4)$ and a small β.

The response of the Langevin model $(N=1)$ will be discussed to an applied spike of $I^{(e)}(t)$ given by Eq. (2) with $A(=0.5)$, $t_{\rm in}(=100)$, and $T_w(=10)$. Figures 3(a) and 3(b) show the time courses of $\mu(t)$ and $\gamma(t,t)(=\rho(t,t))$, respectively, with a set of parameters of $a=1$, $w=0.5$, $\beta=0.001$, and $N=1$, an input spike of $I^{(e)}(t)$ being shown at the bottom of Fig. 3(a). Note that results calculalted for different parameters are

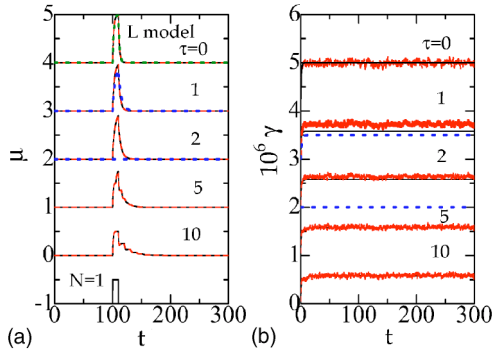

FIG. 3. (Color online) The time course of (a) $\mu(t)$ and (b) $\gamma(t,t)$ of the L model for an applied single spike shown at the bottom frame in (a), calculated in AMM (solid curves), the small-delay approximation (SDA; dotted curves) and direct simulations (DS; dashed curves) with $a=1$, $w=0.5$, $\beta=0.001$, and $N=1$: results of $\mu(t)$ for AMM and DS are indistinguishable, and results of SDA are shown only for $\tau\leqslant 2$ (see the text).

vertically shifted for clarity in Fig. 3 (also in Figs. 4, 7, and 8). When an input spike is applied at $t=100$, state variables of $x_i(t)$ are randomized because independent noises have been added since $t=0$. Solid and dashed curves in Fig. 3(a), which denote results of AMM and DSs, respectively, are practically identical. The dotted curve expressing $\mu(t)$ of SDA is in fairly good agreement with that of DSs for $\tau=1$, but the former completely disagrees with the latter for $\tau\geqslant 2$. We should note in Eqs. (20)–(23) that $\mu(t)$ is decoupled from $\gamma(t,t)$ and $\rho(t,t)$, then $\gamma(t,t)$ is independent of an external input $I^{(e)}(t)$. Figure 3(b) shows that time courses of $\gamma(t,t)$ of AMM and DS are almost identical for $\tau=0$. For $\tau=1$, the result of the AMM is underestimated compared to that of DS as discussed before. However, an agreement of the result of AMM with that of DS becomes better for $\tau\geqslant 4$. Results of $\gamma(t,t)$ of DS at large t (>100) are in good agreement with the exact stationary solution of γ^* shown in Fig. 2(c).

2. N>1 case

We will discuss dynamics, in particular the synchronization, of ensembles for $N>1$. In order to monitor the synchronization, we consider the quantity given by [19]

$$R(t) = \frac{1}{N^2}\sum_i \langle [x_i(t)-x_j(t)]^2\rangle = 2[\gamma(t,t)-\rho(t,t)]. \tag{26}$$

When all neurons are in the completely synchronous states, we get $x_i(t)=X(t)$ for all i and then $R(t)=0$. In contrast, in the asynchronous states, we get $R(t)=2(1-1/N)\gamma(t,t)\equiv R_0(t)$ because $\rho(t,t)=\gamma(t,t)/N$ [Eq. (16)]. The *synchronization ratio* $S(t)$ is defined by [19]

$$S(t) = 1-\frac{R(t)}{R_0(t)} = \left(\frac{N\rho(t,t)/\gamma(t,t)-1}{N-1}\right), \tag{27}$$

which becomes 1 (0) for completely synchronous (asynchronous) states. The synchrony σ_s of the ensemble is defined by

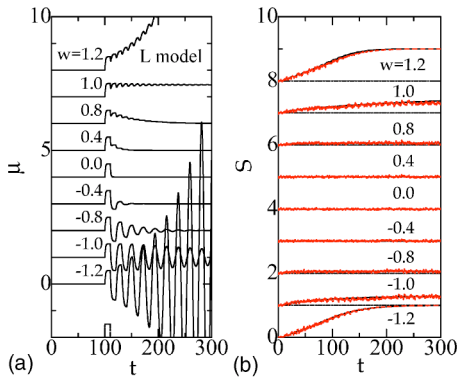

FIG. 4. (Color online) Time courses of (a) $\mu(t)$ and (b) $S(t)$ of the L model calculated by AMM (solid curves) and DS (dashed curves) for various w with $\tau=10$, $\beta=0.001$ and $N=10$: results of $\mu(t)$ for AMM and DS are indistinguishable. The chain curve at the bottom of (a) expresses an applied input spike.

$$\sigma_s = \overline{S(t)} = \left(\frac{1}{t_2 - t_1}\right)\int_{t_1}^{t_2} dt\, S(t), \tag{28}$$

where the overline denotes the temporal average between times t_1 (=2000) and t_2 (=3000).

Figures 4(a) and 4(b) show the time course of $\mu(t)$ and $S(t)$, respectively, for various w with $\tau=10$, $\beta=0.001$, and $N=10$, solid and dashed curves denoting results of AMM and DS, respectively. For $w=0$, $\mu(t)$ behaves as a simple relaxation process with the relaxation time of $\tau_r=1/a=1$, while $S(t)$ is vanishing. When a small, positive coupling of $w=0.4$ is introduced, $\mu(t)$ shows the stairlike structure because of the positive delayed feedback. The synchronization ratio $S(t)$ for $w=0.4$ shows a gradual development as increasing t, but the magnitude of its averaged value of σ_s is very small ($\sim$0.015). When w is more increased to $w=0.8$, the effective relaxation time for $\mu(t)$ to return to the initial zero value becomes larger and σ_s becomes also larger. For $w=1.0$, the effective relaxation time becomes infinity and $\mu(t)$ remains at the finite value of $\mu(t)=0.455$. For $w>1$, the divergence in $\mu(t)$ is triggered by an input spike and $S(t)$ tends to a fully synchronized state of $\sigma_s=1$. On the contrary, for a small negative coupling of $w=-0.4$, $\mu(t)$ shows an ostensibly quasi-oscillating state because of negative delayed feedback. With increasing magnitude of negative w, the term showing this quasi-oscillation becomes longer. For $w<-1.2$, $\mu(t)$ shows a divergent oscillation and $S(t)$ tends to saturate at unity for $t>250$.

The w dependence of σ_s, which is the temporal average of $S(t)$, is depicted in Fig. 5(a), where solid and dashed curves show results of AMM and DS with 1000 trials, respectively: error bars showing the root-mean-square (RMS) value of DS are within the radius of circles. Although σ_s is very small for $|w|<0.9$, it is suddenly increased as $|w|$ approaches the unity, where the divergence of the autonomous oscillation is induced as shown in Fig. 4(a).

The delay time τ plays an important role, as discussed before in the case of $N=1$ [Fig. 2(b)]. Figure 5(b) shows the τ dependence of σ_s calculated by AMM (the solid curve) and

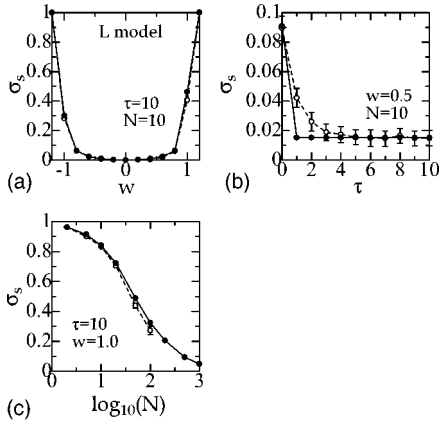

FIG. 5. (a) The w dependence of σ_s, the temporal average of $S(t)$, of the L model calculated in AMM (the solid curve) and DS with $N_r=1000$ (the dashed curve) for $\tau=10$, $\beta=0.001$, and $N=10$. (b) The τ dependence of σ_s for $w=0.5$, $\beta=0.001$, and $N=10$ calculated by AMM (the solid curve) and DS with $N_r=1000$ (the dashed curve). (c) The N dependence of σ_s for $w=1.0$, $\tau=10$, and $\beta=0.001$ calculated by AMM (the solid curve) and DS (the dashed curve); $N_r=100$ for $N=50$ and 100, and $N_r=1000$ otherwise. Error bars denote RMS values of DS.

DS with 1000 trials (the dashed curve) for $w=0.5$, $\beta=0.001$, and $N=10$. We note that $\sigma_s=0.091$ for $\tau=0$ is rapidly decreased with increasing τ from zero, while it is almost constant at $\tau>4$. This τ dependence of σ_s resembles that of γ^* for $N=1$ shown in Fig. 2(a).

We have so far fixed the size of N, which is now changed. Figure 5(c) shows the N dependence of σ_s calculated in AMM (the solid curve) and DS (the dashed curve) for $\tau=10$, $w=1.0$, and $\beta=0.001$. For $N=2$, the synchronization of $\sigma_s\sim0.963$ is nearly complete. With increasing N, however, σ_s is gradually decreased: $\sigma_s=0.824$ and 0.340 for $N=10$ and 100, respectively.

Model calculations have shown that in linear Langevin ensembles with appropriate model parameters, an applied spike induces oscillations with divergent amplitudes. This is contrast with the nonlinear Langevin ensembles where stable oscillations with finite amplitudes are possible, as will be shown in the following Sec. III B.

B. Nonlinear model

Next we consider the nonlinear (NL) model in which $F(x)$ and $H(x)$ in Eq. (1) are given by

$$F(x) = -ax, \tag{29}$$

$$H(x) = x - bx^3 \quad (a \geqslant 0, b > 0). \tag{30}$$

The NL model given by Eqs. (1), (29), and (30) with $a=0$, $b=1$, $I^{(e)}(t)=0$, and $N=1$ has been discussed in Ref. [10]. With the use of Eqs. (29) and (30), Eqs. (7)–(10) become

$$\frac{d\mu(t)}{dt} = -a\mu(t) + wu_0(t-\tau) + I^{(e)}(t), \tag{31}$$

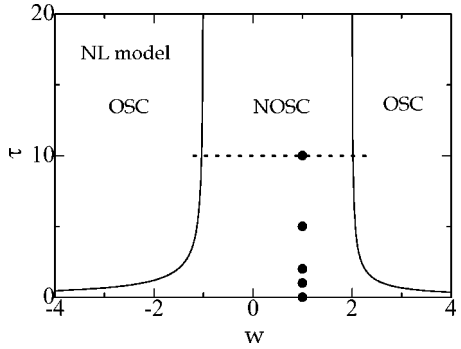

FIG. 6. The $w-\tau$ phase diagram of the nonlinear (NL) model given by Eqs. (29) and (30) with $a=1$, $b=1/6$, and $\beta=0$, showing the nonoscillating (NOSC) and oscillating (OSC) states. Calculations whose results are depicted in Fig. 7, are performed for sets of parameters shown by circles. Along the horizontal dotted lines, the w value is changed for calculations shown in Figs. 8 and 9(a)–9(c) (see text).

$$\frac{d\gamma(t,t)}{dt} = -2a\gamma(t,t) + 2wu_1(t-\tau)\rho(t,t-\tau) + \beta^2, \quad (32)$$

$$\frac{d\rho(t,t)}{dt} = -2a\rho(t,t) + 2wu_1(t-\tau)\rho(t,t-\tau) + \frac{\beta^2}{N}, \quad (33)$$

$$\frac{d\rho(t,t-m\tau)}{dt} = -2a\rho(t,t-m\tau) + wu_1(t-(m+1)\tau) \times\rho(t,t-(m+1)\tau) + wu_1(t-\tau)\rho(t-\tau,t-m\tau) + \frac{\beta^2}{N}\Delta(m\tau), \quad (\text{for } m \geq 1), \quad (34)$$

with

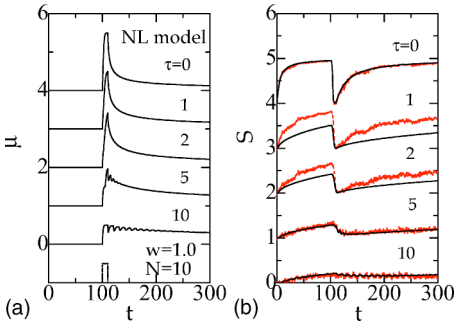

FIG. 7. (Color online) The time course of (a) $\mu(t)$ and (b) $S(t)$ of the NL model for an applied single spike shown at the bottom frame in (a), calculated in AMM (solid curves) and DS (dashed curves) for $a=1$, $b=1/6$, $w=1.0$, $\beta=0.001$, and $N=10$: results of $\mu(t)$ for AMM and DS are indistinguishable.

$$u_0(t) = \mu(t) - b\mu(t)^3 - 3b\mu(t)\gamma(t,t), \quad (35)$$

$$u_1(t) = 1 - 3b\mu(t)^2 - 3b\gamma(t,t). \quad (36)$$

For $\beta=0$ and $I^{(e)}(t)=0$, Eq. (31) has the stationary solution given by

$$\mu^* = 0 \quad \text{for } w < a \quad (37)$$

$$= \pm\sqrt{\frac{w-a}{bw}} \quad \text{for } w > a. \quad (38)$$

Linearizing Eq. (31) around μ^*, we get the condition for the stable stationary solution given by

$$\tau < \tau_{c1} = \frac{\cos^{-1}(a/w)}{\sqrt{(w^2-a^2)}} \quad \text{for } w < a, \quad (39)$$

$$< \tau_{c2} = \frac{\cos^{-1}[a/(3a-2w)]}{\sqrt{[(3a-2w)^2-a^2]}} \quad \text{for } w > 2a. \quad (40)$$

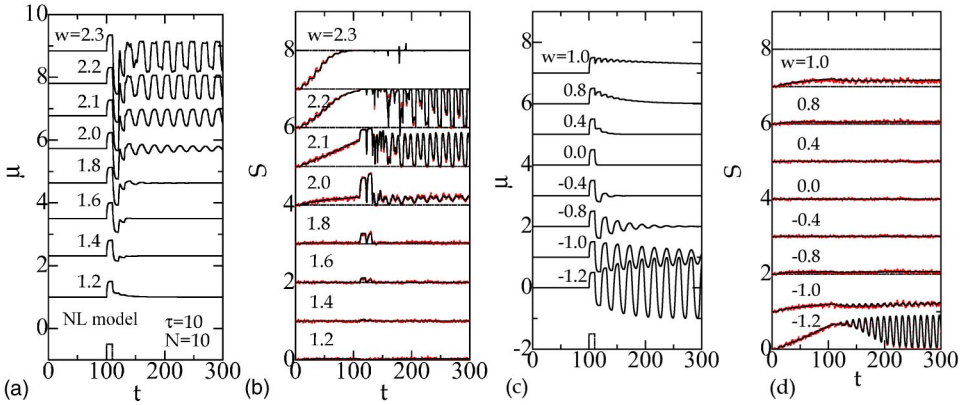

FIG. 8. (Color online) Time courses of (a) $\mu(t)$ and (b) $S(t)$ for $1.2 \leqslant w \leqslant 2.3$, and (c) $\mu(t)$ and (d) $S(t)$ for $-1.2 \leqslant w \leqslant 1.0$, of the NL model calculated by AMM (solid curves) and DS (dashed curves) with $\tau=10$, $\beta=0.001$, and $N=10$: results of $\mu(t)$ for AMM and DS are indistinguishable. Chain curves at bottoms of (a) and (c) express applied input spikes.

Figure 6 shows the calculated $w-\tau$ phase diagram of the NL model, showing the nonoscillating (NOSC) and oscillating states (OSC) with $a=1$ and $b=1/6$, which are adopted for a later comparison with the nonlinear model given by Eqs. (43) and (44) in Sec. IV. When an external spike given by Eq. (2) is applied to the NOSC state, the state is once excited and returns to the stationary state after the transient period, as will be discussed shortly [Figs. 8(a)–8(d)]. On the contrary, when a spike is applied to the OSC state, it induces the autonomous oscillation.

Adopting parameters of w and τ values shown by circles in Fig. 6, we have made calculations for the NL model by AMM and DS, whose results of $\mu(t)$ and $S(t)$ are depicted in Figs. 7(a) and 7(b), respectively, with $\beta=0.001$ and $N=10$, solid and dashed curves expressing results of AMM and DS, respectively. Hereafter we show results of AMM6 whose validity for the NL model will be confirmed later [Fig. 9(b)]. Figure 7(a) shows that with increasing τ, $\mu(t)$ shows the complicated time dependence due to delayed feedbacks. The time course of $\mu(t)$ for $N=10$ is the same as that for $N=1$ (results not shown). As was discussed in Sec. III A, $\gamma(t,t)$ and $\rho(t,t)$ in the L model are independent of an input signal $I^{(e)}(t)$ because they are decoupled from $\mu(t)$ in Eqs. (20)–(23). It is not the case in the NL model, where $\mu(t)$, $\gamma(t,t)$, and $\rho(t,t)$ are coupled each other in Eqs. (31)–(34), and $S(t)$ depends on $I^{(e)}(t)$. Figure 7(b) shows that, for example, in the case of $\tau=0$, $S(t)\sim 0.95$ at $t\leqslant 100$ is suddenly decreased to $S(t)\sim 0$ at $t=100$ by an applied spike, and then it is gradually increased to the stationary value of $S^*\sim 1.0$ at $t>1000$. This trend is realized in all the cases shown in Fig. 7(b). We note that an agreement of $S(t)$ between AMM and DS is good for $\tau=0$, 5, and 10, but not good for $\tau=1$ and 2, just as in the case of the L model [Fig. 2(a)].

Figures 8(a)–8(d) show the time courses of $\mu(t)$ and $S(t)$ when the w value is changed along the horizontal dotted line in Fig. 6, solid and dashed curves denoting results of AMM and DS, respectively. From comparisons among Figs. 4(a), 4(b), and 8(a)–8(d), we note that for $|w|\leqslant 0.8$, time courses of $\mu(t)$ and $S(t)$ of the NL model are similar to those of the L model. The difference between the L and NL models is, however, clearly realized in cases of $|w|\geqslant 1.2$. For $w=-1.2$, $\mu(t)$ in the NL model oscillates with the bounded magnitude [Fig. 8(c)] while $\mu(t)$ in the L model oscillates with divergent magnitude [Fig. 4(a)] although the oscillating period is the same ($T=22$) for L and NL models. In contrast, $S(t)$ in the NL model oscillates [Fig. 8(d)] while $S(t)$ in the L model saturates at unity [Fig. 4(b)]. For $w=1.2$, $\mu(t)$ in the NL model starting from the stationary state with $\mu^*=1.0$, is slightly modified by an input spike applied at $t=100$ with a small magnitude of $S^*=0.024$ for $S(t)$, whereas $\mu(t)$ in the L model shows an unbounded oscillation and $S(t)$ saturates at $S^*=1$. Figure 8(a) shows that as increasing w above 1.2, $\mu(t)$ shows a quasi-oscillation triggered by inputs, by which $S(t)$ is increased at $110\lesssim t\lesssim 130$. For $w>2.0$, the autonomous oscillation with a period of $T=22$ is induced and $S(t)$ is also oscillating with a period of $T=11$.

As discussed above, the oscillation is triggered by an input spike when parameters are appropriate. In order to study the transition between the NOSC and OSC states in more detail, we have calculated the quantity σ_o defined by [31]

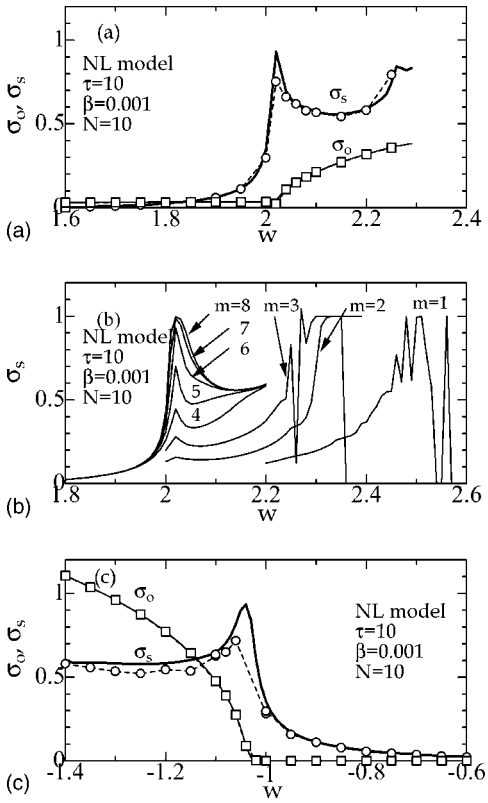

FIG. 9. (a) The w dependence of σ_o and σ_s for $1.6\leqslant w\leqslant 2.4$ of the NL model. (b) The w dependence of σ_s for $1.8\leqslant w\leqslant 2.6$ with different level m in AMMm (see text). (c) The w dependence of σ_o and σ_s for $-1.4\leqslant w\leqslant -0.6$. Solid and dashed curves in (a) and (c) express results of AMM6 and DS calculated with (AMMm), $\beta=0.001$, and $N=10$. Note that the result with $m=6$ in (b) corresponds to the AMM result of σ_s in (a). Errors bars expressing RMS values are not shown for a clarity of figures (see Fig. 10).

$$\sigma_o=\overline{\frac{1}{N}\sum_i\left[\langle x_i(t)^2\rangle-\langle x_i(t)\rangle^2\right]} \tag{41}$$

$$=\overline{\mu(t)^2}-\overline{\mu(t)}^2+\overline{\gamma(t,t)}, \tag{42}$$

which becomes finite in the OSC state but vanishes (or is small) in the NOSC state, the overline denoting the temporal average [Eq. (28)].

Figure 9(a) shows σ_o and σ_s calculated with changing w from 1.6 to 2.4 along the horizontal dotted line in Fig. 6 with $\tau=10$, $\beta=0.001$, and $N=10$, solid and dashed curves denoting results of AMM6 and DS, respectively. The oscillation is triggered by an input spike when w exceeds the critical value of $w_c(\sim 2.02)$. The transition is of the second order since σ_o is continuously increased as $(w-w_c)$ is increased. We should note that the peak in σ_s shows the *fluctuation-induced* enhancement at $w\sim w_c$, which arises from an increase in the ratio of $\rho(t,t)/\gamma(t,t)$ although both $\gamma(t,t)$ and $\rho(t,t)$ are increased. When w exceeds about 2.3, the oscillation becomes irregular, which is expected to be a precursor of the chaotic state.

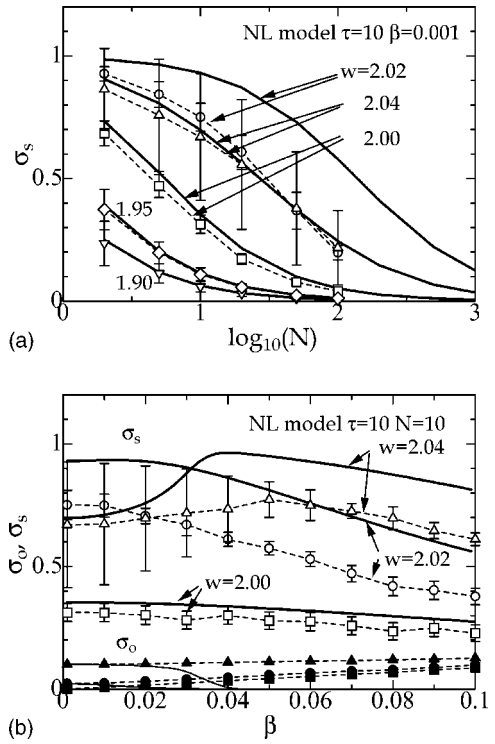

FIG. 10. (a) The N dependence of σ_s for $\tau=10$ and $\beta=0.001$, and (b) the β dependence of σ_s for $\tau=10$ and $N=10$ of the NL model, calculated by AMM (solid curves) and DS (dashed curves) with $w=2.04$ (triangles), 2.02 (circles), 2.0 (squares), 1.95 (diamonds), and 1.90 (inverted triangles). Errors bars expressing RMS values of σ_s of DS, are significant in the OSC state because of the oscillation of $S(t)$.

For calculations of the NL model given by Eqs. (29) and (30), we have adopted AMM6, whose validity is examined in Fig. 9(b) showing σ_s for $1.8 \leqslant w \leqslant 2.6$ when the level m is changed in AMMm: note that the result of $m=6$ in Fig. 9(b) is nothing but the AMM result of σ_s in Fig. 9(a). The critical coupling for the NOSC-OSC transition calculated by AMMm for $m=1-3$ is too large compared to that by DS ($w_c=2.02$) shown in Fig. 9(a). For $m=4$, we get a reasonable value of w_c, but the peak value of σ_s at $w=w_c$ is too small. With furthermore increasing the m value, the w-dependence of σ_s becomes in better agreement with that of DS. The optimum value of m is expected to depend on the model parameters, the required accuracy and the ability of computer facility. Making a compromise among these factors, we have decided to adopt AMM6 in all our calculations. This choice of $m=6$ has been confirmed by results of AMM which are in good agreement with those of DS [Fig. 9(a)].

Figure 9(c) expresses the w dependence of σ_o and σ_s near the NOSC-OSC transition for a negative w when the w value is changed from -1.4 to -0.6 along the horizontal dotted line in Fig. 6. The oscillation is triggered by an input spike when w is below the critical value of $w_c(\sim -1.04)$. The fluctuation-induced enhancement is again realized in σ_s calculated by AMM and DS.

The N-dependence of σ_s has been studied for various $w(\sim 2)$ with $\tau=10$ and $\beta=0.001$, whose results are depicted in Fig. 10(a). It is noted that σ_s with $w=2.02$ is larger than that with $w=2.04$ for all N values, just as shown in Fig. 9(a). With increasing N, σ_s is gradually decreased for all w values. Although RMS values of σ_s in the NOSC state are small, they become considerable in the OSC states, which is due to oscillations in $S(t)$ but not due to noises. In contrast, the N-dependence of σ_o is very small for the parameters investigated (results not shown).

Figure 10(b) shows the β dependence of σ_o and σ_s for $w=2.0$, 2.02, and 2.04 with $\tau=10$ and $N=10$. For $w=2.02$, which is just the critical coupling for $\beta=0.001$ [Fig. 9(a)], σ_s is gradually decreased with increasing β. For $w=2.00(\lesssim w_c)$, σ_s is little decreased with an increase in β. In contrast, for $w=2.04$, σ_s is first increased with increasing w and has a broad peak at $\beta \sim \beta_c$ where $\beta_c=0.04$ in AMM and 0.06 in DS. This broad peak in σ_s may suggest that the OSC state is suppressed by noises although σ_o calculated in DS remains finite at $\beta > \beta_c$, showing no signs for the NOSC-OSC transition. It may be possible that the emergence of the oscillation is not well represented by σ_o defined by Eqs. (41) and (42) in the case of a large β. The discrepancy between results of AMM and DS becomes significant with increasing β, which is due to a limitation of AMM based on the weak-noise assumption.

It has been shown that when model parameters of w, τ, β, and N are appropriate, the stable oscillations with finte magnitudes are induced in NL Langevin ensembles. The fluctuation-induced enhancement is realized in the synchrony near the second-order transition between the NOSC and OSC states.

IV. CONCLUSIONS AND DISCUSSIONS

We may adopt a nonlinear Langevin model given by Eq. (1) with

$$F(x) = -ax \quad (a \geqslant 0), \tag{43}$$

$$H(x) = \sin(x), \tag{44}$$

which is referred to as the NL' model. Equations (43) and (44) were previously employed by Ikeda and Matsumoto [1] for a study on chaos in time-delayed systems. By using Eqs. (43) and (44), and the relation given by

$$H^{(2n)}(t) = (-1)^n \sin(x), \tag{45}$$

$$H^{(2n+1)}(t) = (-1)^n \cos(x), \tag{46}$$

we get DEs given by Eqs. (31)–(34) but with

$$u_0(t) = \sin(\mu(t))\exp\left(-\frac{\gamma(t,t)}{2}\right), \tag{47}$$

$$u_1(t) = \cos(\mu(t))\exp\left(-\frac{\gamma(t,t)}{2}\right), \tag{48}$$

where all contributions from $n=0$ to ∞ in Eqs. (11)–(14) are included. It is noted that Eq. (30) with $b=1/6$ is an approximate form of Eq. (44) for a small x. Correspondingly, $u_0(t)$ and $u_1(t)$ given by Eqs. (35) and (36) are approximate ex-

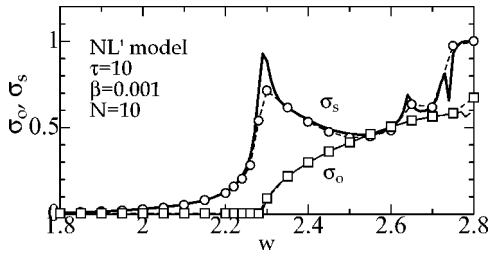

FIG. 11. The w dependence of σ_o and σ_s of the NL' model given by Eqs. (43) and (44), calculated by AMM (solid curves) and DS (dashed curves) with $\tau=10$, $\beta=0.001$, and $N=10$ (see text). Error bars expressing RMS values are not shown for a clarity of the figure.

pressions of those given by Eqs. (47) and (48), respectively, for small $\mu(t)$ and $\gamma(t,t)$.

Figure 11 shows the w dependence of σ_o and σ_s of the NL' model. The NOSC-OSC transition occurs at $w_c=2.29$ above which σ_o is continuously increased and where σ_s has a peak. Although the induced oscillation is regular for $2.29 \leqslant w \lesssim 2.64$, it becomes irregular for $w \gtrsim 2.64$, which may lead to the bifurcation and chaos [1]. We note from Figs. 9(a) and 11 that the w dependence of the NL model given by Eqs. (29) and (30) is similar to that of the NL' model given by Eqs. (43) and (44) although the critical coupling for the NOSC-OSC is different between the two models. The $w-\tau$ phase diagram for the NL' Langevin model is almost the same as that for NL Langevin ensembles shown in Fig. 6. Recently the phase diagram has been experimentally obtained for a coupled *pair* of the plasmodium of the slime mold, *physarum polycephalum*, where the coupling strength and delay time are systematically controlled [32]. The observed phase diagram is not dissimilar to our $w-\tau$ phase diagrams for NL and NL' Langevin models as far as unentrained and in-phase oscillating states are concerned.

Quite recently, Huber and Tsimring (HT) [17] have discussed an alternative nonlinear Langevin ensembles given by Eq. (1) with

$$F(x) = x - x^3, \tag{49}$$

$$H(x) = x, \tag{50}$$

for $I^{(e)}(t)=0$, which expresses interconnected bistable systems with delays [14]. By using DSs and analytical methods based on the Gaussian and dichotomous approximations, HT have discussed the coherence resonance and multistability of the system. When we apply our approximation to this nonlinear model, Eqs. (7)–(10) become

$$\frac{d\mu(t)}{dt} = \mu(t) - \mu(t)^3 - 3\mu(t)\gamma(t,t) + w\mu(t-\tau) + I^{(e)}(t), \tag{51}$$

$$\frac{d\gamma(t,t)}{dt} = 2[1 - 3\mu(t)^2 - 3\gamma(t,t)]\gamma(t,t) + 2w\rho(t,t-\tau) + \beta^2, \tag{52}$$

$$\frac{d\rho(t,t)}{dt} = 2[1 - 3\mu(t)^2 - 3\gamma(t,t)]\rho(t,t) + 2w\rho(t,t-\tau) + \frac{\beta^2}{N}, \tag{53}$$

$$\frac{d\rho(t,t-m\tau)}{dt} = [g_1(t) + g_1(t-m\tau)]\rho(t,t-m\tau) + w\rho(t,t-(m+1)\tau) + w\rho(t-\tau,t-m\tau) + \frac{\beta^2}{N}\Delta(m\tau) \quad (\text{for } m \geqslant 1), \tag{54}$$

where $g_1(t)=1-3\mu(t)^2-3\gamma(t,t)$. In their Gaussian approximation, HT have employed Eqs. (51) and (52) with $\rho(t,t-\tau)=0$, discarding Eqs. (53) and (54). It has been claimed that the Gaussian approximation is not adequate near the transition point between the ordered and disordered states, although a dichotomous theory yields a fairly good description. This might be due to a neglect of the higher-order contributions in Eqs. (52)–(54), which are expected to play important roles, in particular, near the transition point, as our calculations have shown [Fig. 9(b) and Fig. 5(b) of Ref. [26] for FN neuron models].

In summary, we have proposed a semianalytical approach for a study of dynamics of stochastic ensembles described by linear and nonliner Langevin models with delays. Advantages of our method are (a) the synchronization in ensembles may be discussed by taking into account correlations of local and global variables, (b) the recursive DEs terminated at finite $m(\sim 6)$ yield fairly good results compared to those of DSs, and (c) our method is free from the magnitude of time delays though the noise intensity is assumed to be weak, which is complementary to SDA [9]. The proposed method is expected to be useful not only to Langevin ensembles but also to more general stochastic ensembles with delays. Although our method is applicable to the system with an arbitrary size of N, it is better applied to larger system because of its mean-field nature. It should be noted that the number of DEs to be solved for N-unit stochastic Langevin model is NN_r in DS with N_r trials, while it is $(m+3)$ in AMMm. The ratio between the two numbers becomes $NN_r/(m+3) \sim 1000$, for example, for $N=N_r=100$ and $m=6$. Actually this reflects on the ratio of the speed for numerical computations by using the two methods. Taking these advantages of our method, we have applied it to ensembles described by the FN neuron model with delayed couplings to study their dynamics and synchronization, which are reported in a following paper [26].

ACKNOWLEDGMENT

This work was partly supported by a Grant-in-Aid for Scientific Research from the Japanese Ministry of Education, Culture, Sports, Science, and Technology.

APPENDIX A: DERIVATION OF EQS. (7)–(10)

Assuming that the noise intensity β is small, we express Eq. (1) in a Taylor expansion of δx_i as

$$\frac{dx_i(t)}{dt} = \sum_{\ell=0}^{\infty} \frac{F^{(\ell)}(t)}{\ell!} \delta x_i(t)^{\ell} + \frac{w}{N} \sum_j \sum_{\ell=0}^{\infty} \frac{H^{(\ell)}(t-\tau)}{\ell!} \delta x_j(t-\tau)^{\ell} + \xi_i(t) + I^{(e)}(t), \tag{A1}$$

where $F^{(\ell)}(t) = F^{(\ell)}(\mu(t))$ and $H^{(\ell)}(t) = H^{(\ell)}(\mu(t))$. Equations (3), (4), and (A1) yield DE for means of $\mu(t)$ as

$$\frac{d\mu(t)}{dt} = \frac{1}{N} \sum_i \sum_{\ell=0}^{\infty} \frac{F^{(\ell)}(t)}{\ell!} \langle \delta x_i(t)^{\ell} \rangle + \frac{w}{N^2} \sum_i \sum_j \sum_{\ell=0}^{\infty} \frac{H^{(\ell)}(t-\tau)}{\ell!} \langle \delta x_j(t-\tau)^{\ell} \rangle + I^{(e)}(t). \tag{A2}$$

When we adopt the Gaussian decoupling approximation, averages higher than the second-order moments in Eq. (A2) may be expressed in terms of the second-order moments given by

$$\langle \delta x_1, \ldots, \delta x_\ell \rangle = \sum_{\text{all pairings}} \Pi_{km} \langle \delta x_k \delta x_m \rangle \quad \text{for even } \ell$$
$$= 0 \quad \text{for odd } \ell, \tag{A3}$$

where the summation is performed for all $(\ell-1)(\ell-3)\cdots 3\cdot 1$ combinations. With the use of the Gaussian decoupling approximation given by Eq. (A3), Eq. (A2) becomes

$$\frac{d\mu(t)}{dt} = \frac{1}{N} \sum_i \sum_{n=0}^{\infty} \frac{F^{(2n)}(t)}{(2n)!} B_{2n} \langle \delta x_i(t)^2 \rangle^n + \frac{w}{N^2} \sum_i \sum_j \sum_{n=0}^{\infty} \frac{H^{(2n)}(t-\tau)}{(2n)!} B_{2n} \langle \delta x_j(t-\tau)^2 \rangle^n + I^{(e)}(t), \tag{A4}$$

where $B_{2n} = (2n-1)(2n-3)\cdots 3\cdot 1$. Adopting the mean-field approximation given by

$$\langle \delta x_i(t)^2 \rangle^n \simeq \gamma(t,t)^{n-1} \langle \delta x_i(t)^2 \rangle, \tag{A5}$$

we get

$$\frac{d\mu(t)}{dt} = \sum_{n=0}^{\infty} \frac{F^{(2n)}(t)}{n!} \left(\frac{\gamma(t,t)}{2} \right)^n + w \sum_{n=0}^{\infty} \frac{H^{(2n)}(t-\tau)}{n!} \left(\frac{\gamma(t-\tau,t-\tau)}{2} \right)^n + I^{(e)}(t), \tag{A6}$$

which yields Eqs. (7), (11), and (13).

From Eqs. (A1) and (A4), we gt DEs for $d\delta x_i(t)/dt$ as

$$\frac{d\delta x_i(t)}{dt} = \frac{dx_I(t)}{dt} - \frac{d\mu(t)}{dt} \tag{A7}$$

$$= \sum_{n=0}^{\infty} F^{(2n+1)}(t) \frac{\delta x_i(t)^{2n+1}}{(2n+1)!} + \sum_{n=0}^{\infty} F^{(2n)}(t) \left(\frac{\delta x_i(t)^{2n}}{(2n)!} - \frac{\gamma(t,t)^n}{2^n n!} \right) + \frac{w}{N} \sum_j \sum_{n=0}^{\infty} H^{(2n+1)}(t-\tau) \frac{\delta x_j(t-\tau)^{2n+1}}{(2n+1)!} + \frac{w}{N} \sum_j \sum_{n=0}^{\infty} H^{(2n)}(t-\tau) \times \left(\frac{\delta x_j(t-\tau)^{2n}}{(2n)!} - \frac{\gamma(t-\tau,t-\tau)^n}{2^n n!} \right) + \xi_i(t). \tag{A8}$$

By using Eqs. (5), (A3), and (A8), we get DEs for $d\gamma(t,t)/dt$ as

$$\frac{d\gamma(t,t)}{dt} = \frac{2}{N} \sum_i \left\langle \delta x_i(t) \frac{d\delta x_i(t)}{dt} \right\rangle \tag{A9}$$

$$= \frac{2}{N} \sum_j \sum_{n=0}^{\infty} \frac{F^{2n+1}(t)}{(2n+1)!} \langle \delta x_i(t)^{2n+2} \rangle + \frac{2w}{N^2} \sum_i \sum_j \sum_{n=0}^{\infty} \frac{H^{2n+1}(t-\tau)}{(2n+1)!} \langle \delta x_i(t) \delta x_j(t-\tau)^{2n+1} \rangle + \frac{2}{N} \sum_i \langle \delta x_i(t) \xi_i(t) \rangle$$
$$= \frac{2}{N} \sum_i \sum_{n=0}^{\infty} \frac{F^{2n+1}(t)}{(2n+1)!} B_{2n+2} \langle \delta x_i(t)^2 \rangle^{n+1} + \frac{2w}{N^2} \sum_i \sum_j \sum_{n=0}^{\infty} \frac{H^{2n+1}(t-\tau)}{(2n+1)!} B_{2n+2} \langle \delta x_i(t) \delta x_j(t-\tau) \rangle \times \langle \delta x_j(t-\tau)^2 \rangle^n + \beta^2. \tag{A10}$$

With the use of the mean-field approximation given by Eq. (A5), Eq. (A10) reduces to

$$\frac{d\gamma(t,t)}{dt} = 2\gamma(t,t) \sum_{n=0}^{\infty} \frac{F^{(2n+1)}(t)}{n!} \left(\frac{\gamma(t,t)}{2} \right)^n + 2w\rho(t,t-\tau) \times \sum_{n=0}^{\infty} \frac{H^{(2n+1)}(t-\tau)}{n!} \left(\frac{\gamma(t-\tau,t-\tau)}{2} \right)^n + \beta^2, \tag{A11}$$

leading to Eqs. (8), (12), and (14). Calculations of $d\rho(t,t)/dt$ and $d\rho(t,t-m\tau)/dt$ are similarly performed by using the relation:

$$\frac{d\rho(t,t-m\tau)}{dt} = \frac{1}{N^2} \sum_i \sum_j \left\langle \delta x_i(t) \frac{dx_j(t-m\tau)}{dt} + \frac{dx_i(t)}{dt} x_j(t-m\tau) \right\rangle. \tag{A12}$$

In the process of calculating $d\rho(t,t-m\tau)/dt$, we get new correlation functions given by

$$S(t,t-m\tau)=\frac{1}{N}\sum_i \langle \delta x_i(t)\xi_i(t-m\tau)\rangle, \tag{A13}$$

$$S(t-m\tau,t)=\frac{1}{N}\sum_i \langle \delta x_i(t-m\tau)\xi_i(t)\rangle. \tag{A14}$$

By using the method of steps in Ref. [13], we get

$$S(t,t-m\tau)=S(t-m\tau,t)=\left(\frac{\beta^2}{2}\right)\Delta(m\tau), \tag{A15}$$

which leads to Eq. (10).

APPENDIX B: THE SMALL-DELAY APPROXIMATION

We apply the small-delay approximation (SDA) first proposed in Ref. [9] to our model given by Eqs. (1) and (2). When τ is small, we may expand Eq. (1) for $N=1$ as $x(t-\tau)\sim x(t)-\tau dx(t)/dt$ to get

$$\frac{dx(t)}{dt}\simeq F(x(t))+w\left(H(x(t))-\tau H'(x(t))\frac{dx(t)}{dt}\right)+\beta\eta(t)+I^{(e)}(t). \tag{B1}$$

Using Eq. (B1), we get DEs for $\mu(t)$ and $\gamma(t,t)$ given by

$$\frac{d\mu(t)}{dt}=[1-w\tau h_1(t)][g_0(t)+wu_0(t)+I^{(e)}(t)], \tag{B2}$$

$$\frac{d\gamma(t,t)}{dt}=2[1-w\tau h_1(t)][g_1(t)+wu_1(t)]\gamma(t,t)+[1-w\tau h_1(t)]^2\beta^2, \tag{B3}$$

where $h_1(t)=H'(\mu(t))$. For the L model given by Eqs. (1), (2), (18), and (19), Eqs. (B2) and (B3) become

$$\frac{d\mu(t)}{dt}=(1-w\tau)[(-a+w)\mu(t)+I^{(e)}(t)], \tag{B4}$$

$$\frac{\partial\gamma(t,t)}{\partial t}=2(1-w\tau)(-a+w)\gamma(t,t)+(1-w\tau)^2\beta^2. \tag{B5}$$

The τ dependence of the stationary solution of γ^* is shown by the dotted curve in Fig. 2(b). The time course of $\mu(t)$ is plotted by dotted curves in Fig. 3(a).

[1] K. Ikeda, H. Daido, and O. Akimoto, Phys. Rev. Lett. **45**, 709 (1980); K. Ikeda and K. Matsumoto, Physica D **29**, 223 (1987).
[2] M. C. Mackey and L. Glass, Science **197**, 287 (1979).
[3] J. Foss, A. Longtin, B. Mensour, and J. Milton, Phys. Rev. Lett. **76**, 708 (1996).
[4] L. Gammaitoni, P. Hänngi, P. Jung, and F. Marchesoni, Rev. Mod. Phys. **70**, 223 (1998).
[5] J. García-Ojalvo and R. Roy, Phys. Lett. A **224**, 51 (1996); C. Masoller, Phys. Rev. Lett. **86**, 2782 (2001).
[6] A. Longtin, J. G. Milton, J. E. Bos, and M. C. Mackey, Phys. Rev. A **41**, 6992 (1990); Y. Chen, M. Ding, and J. A. Scott Kelso, Phys. Rev. Lett. **79**, 4501 (1997).
[7] U. Küchler and B. Mensch, Stoch. Stoch. Rep. **40**, 23 (1992).
[8] M. C. Mackey and I. G. Nechaeva, Phys. Rev. E **52**, 3366 (1995).
[9] S. Guillouzic, I. L'Heureux, and A. Longtin, Phys. Rev. E **59**, 3970 (1999).
[10] S. Guillouzic, I. L'Heureux, and A. Longtin, Phys. Rev. E **61**, 4906 (2000).
[11] T. Ohira and T. Yamane, Phys. Rev. E **61**, 1247 (2000).
[12] T. D. Frank and P. J. Beek, Phys. Rev. E **64**, 021917 (2001).
[13] T. D. Frank, P. J. Beek, and R. Friedrich, Phys. Rev. E **68**, 021912 (2003).
[14] L. S. Tsimring and A. Pikovsky, Phys. Rev. Lett. **87**, 250602 (2001).
[15] S. Kim, S. H. Park, and C. S. Ryu, Phys. Rev. Lett. **79**, 2911 (1997).
[16] R. Borisyuk, BioSystems **67**, 3 (2002).
[17] D. Huber and L. S. Tsimring, Phys. Rev. Lett. **91**, 260601 (2003).
[18] M. P. Zorzano and L. Vázquez, Physica D **179**, 105 (2003).
[19] H. Hasegawa, Phys. Rev. E **67**, 041903 (2003).
[20] H. Hasegawa, Phys. Rev. E **68**, 041909 (2003).
[21] R. Rodriguez and H. C. Tuckwell, Phys. Rev. E **54**, 5585 (1996).
[22] H. C. Tuckwell and R. Rodriguez, J. Comput. Neurosci. **5**, 91 (1998).
[23] S. Tanabe and K. Pakdaman, Phys. Rev. E **63**, 031911 (2001).
[24] R. FitzHugh, Biophys. J. **1**, 445 (1961); J. Nagumo, S. Arimoto, and S. Yoshizawa, Proc. IRE **50**, 2061 (1962).
[25] A. L. Hodgkin and A. F. Huxley, J. Physiol. (London) **117**, 500 (1952).
[26] H. Hasegawa, Phys. Rev. E **70**, 021912 (2004).
[27] M. Salami, C. Itami, T. Tsumoto, and F. Kimura, Proc. Natl. Acad. Sci. U.S.A. **100**, 6174 (2002).
[28] The bracket of $\langle G(\mathbf{z},t)\rangle$ denotes the average (or the expectation value) of an arbitrary function $G(\mathbf{z},t)$ of N-unit Langevin ensembles, defined by $\langle G(\mathbf{z},t)\rangle=\int\cdots\int d\mathbf{z}\, G(\mathbf{z},t)p(\mathbf{z})$, where $p(\mathbf{z})$ denotes a probability distribution function (pdf) for N-dimensional random variables of $\mathbf{z}=(x_1,\ldots,x_N)^t$.
[29] S. Tanabe, S. Sato, and K. Pakdaman, Phys. Rev. E **60**, 7235 (1999).
[30] S. Tanabe and K. Pakdaman, Biol. Cybern. **85**, 269 (2001).
[31] J. H. E. Cartwright, Phys. Rev. E **62**, 1149 (2000); C. D. E. Boschi, E. Louis, and G. Ortega, *ibid.* **65**, 012901 (2001).
[32] A. Takamatsu, T. Fujii, and I. Endo, Phys. Rev. Lett. **85**, 2026 (2000).